Available online at www.sciencedirect.com

ScienceDirect

Procedia Structural Integrity 68 (2025) 988–1002

Structural Integrity Procedia

www.elsevier.com/locate/procedia

European Conference on Fracture 2024

Computational welding mechanics-based approach for the optimization of process parameters in laser welding of IN792 nickel-base alloy

Paolo Ferro[a*], Alessandra Varone[b], Giuliano Angella[c], Francesco Cognini[d], Roberto Montanari[b], Filippo Berto[e], Franco Bonollo[a], Giusepope Barbieri[d], Fabio Bergamini[d]

[a]*Universiry of Padova, Department of Management and Engineering, Stradella San Nicola 3 36100, Vicenza, Italy*
[b]*University of Rome Tor Vergata, Department of Industrial Engineering, Via del Politecnico 1 00133, Rome, Italy*
[c]*National Research Council of Italy (CNR), Institute of Condensed Matter Chemistry and Technologies for Energy (ICMATE), 20125 Milan, Italy.*
[d]*ENEA, Department for Sustainability-Research Centre of Casaccia, Santa Maria di Galeria, 00123 Rome, Italy*
[e]*University of Rome "La Sapienza", Department of Chemical Engineering Materials Environment, Via Eudossiana 18 00184 Roma, Italy*

Abstract

Welding and repairing of nickel-base alloys and superalloys plays a crucial role in developing a new sustainability-based world. High power density welding is preferred to conventional arc welding because of its lower heat input that minimizes heat-induced alterations to the material. However, when dealing with nickel-base alloys, the challenge is to obtain a sound joint while avoiding the formation of solidification cracks.

The present work is aimed at summarizing the preliminary results of a numerical study about the effects of laser welding parameters on thermal and mechanical fields of IN792 butt-welded joints. The effects of preheating temperature, heat input and welding speed on thermal and residual stress were investigated. Finally, some melt-run trials were carried out and the structural integrity of the obtained samples was discussed based on the numerical results.

Keywords: Laser Welding; IN792; Finite Element Analysis; Residual stress; Computational Welding Mechanics; Solidification Cracking.

* Corresponding author. Tel.: +39-0444-998744.
E-mail address: paolo.ferro@unipd.it

10.1016/j.prostr.2025.06.161

1. Introduction

Repairing is a well-known strategy used in the frame of sustainable metallurgy to enhance above all the lifespan of those products that requires a lot of energy to be produced such as nickel-base turbine blades (Wilson et. al, 2014). Laser welding is an excellent technology particularly suitable for metal repairs as it reduces the area altered by heat to a minimum, allows the fusion of dissimilar metals and can cover cavities resulting from the removal of a possible surface defect through the deposition of filler metal (Rinaldi et al., 1997; Sandy et al., 2000). Unfortunately, some alloys such as Aluminum or nickel-base alloys, suffer from solidification cracking (SC) that is a tremendous but also intriguing challenge to face. The crack forms and grows immediately behind the fusion zone where the alloy is in a semi-solid state or just in a solidified state (sub-solidus weld cracking (David et al. 1997)), due to an unfortunate combination of metallurgical, thermal and mechanical factors. Different works can be found in literature dealing with the SC phenomenon. In their work, Hu and Richardson (2006) studied the transverse solidification cracking phenomenon in aluminum alloys and proposed some strategies to obtain sound welds. For instance, they found that using a lower welding speed in combination with a lower heat input can prevent the SC formation. Alternatively, the use of a secondary source to reduce the cooling rate and therefore the thermal longitudinal stresses in the mushy zone could be used to obtain sound joints. Other mitigating actions against SC, suggested by Norouzian et al. (2023), are the use of grain refiners, laser beam oscillation and ultrasonic vibration. Coniglio and Cross (2020) focused their attention on the influence of welding speed on SC producing three review papers. In the first one they highlighted the opposite effects that increasing welding speed have on SC. In fact, a higher welding speed enhances SC by increasing the crack-susceptible zone (CSZ) length, decreasing the time to feed shrinkage, and generating centerline grain segregation but at the same time it shifts the compression cell to the mushy zone, reducing the time exposed to strain, and refining weld metal grains. In the second work, the authors discuss the importance of selecting properly the metrics, while, in the third paper they detail the different methods to model the effect of welding speed on solidification cracking occurrence.

Among nickel-base alloys, Inconel 792 (IN792) is often selected to produce aircraft gas turbine (jet) engines and therefore is mainly used in the directionally solidified (DS) state, but it can also be found in the equiaxed (E) form. Repairing is highly recommended in these kinds of components because of their high cost. However, repairing by fusion welding is not an easy task due to an embrittlement phenomenon occurring during cooling in a specific range of temperature ("strain-age" cracking). To solve this issue, Suharno and Sugianto (2012) suggest using the arc welding process provided that the component to be repaired is pre-heated and remains during the repair in a temperature range between 500 and 1010 °C. Barbieri et al. (2024) were able to laser weld 2 mm thick plates of IN792, in directionally solidified state, using optimized parameters and a pre-heating of 200 °C. Similar investigations were also carried out by Angella et al. (2017) on the same directionally solidified alloy but using the electron beam source. In that case, cracks-free weldments were obtained using a pre-heating temperature of 300 °C with process parameters as follows: power = 1 kW, acceleration voltage = 50 kV, beam current = 20 mA, welding speed = 41.7 mm/s.

In this scenario, to better understand the influence of process parameters (welding speed, power, pre-heating temperature) on thermal history, thermal and residual stress field, induced by high density welding processes on IN792, a numerical model was developed and used to interpret the structural integrity of data coming from literature and some additionally melt-run trials carried out on equiaxed (E) IN792.

2. Experimental and numerical method

2.1. Material and methods

Table 1 collects the chemical composition of the analyzed alloy, IN792.

Table 1. Chemical composition of IN792.

C	Al	Cr	Ti	Co	Mo	W	O	Ta	Ni
0.39	3.1	11.2	3.9	8.7	1.7	3.8	3.1	4.3	Bal.

The raw material was provided in the form of cylindrical ingots (Φ = 25 mm, L = 60 mm) that underwent to a solubilization heat treatment at 1120 °C for 2 h in vacuum and ageing at 845 °C for 12 h followed by air cooling. 2 mm and 3 mm thick plates were obtained by spark-erosion cutting along the ingot axis. Some bead on plate (BoP) trials were carried out by varying the pre-heating temperature (P-HT), the laser power and the welding speed.

2.2. Numerical model

The numerical model was developed following the computational welding mechanics (CWM) approach that involves the application of the thermal load by applying a power density distribution that simulates the welding source. The source parameters are calibrated using some macrographs of the weld and possibly some thermal histories measured with thermocouples positioned near the weld bead.

To obtain an optimal match between the predicted an experimental fusion zone (FZ) shape and dimension, a combination of two conical shape heat sources, with gaussian power density distribution, was used. The schematic is shown in Fig. 1 while the volumetric power density distributions functions are given in Eq. (1) and (2).

$$Q_1(x,y,z) = \frac{6\beta_1 \cdot P}{\pi H_1 (r_e^2 + r_e r_m + r_m^2)} exp\left(-2\frac{r^2}{r_0^2}\right), \quad r_0(z) = r_e - (r_e - r_m) \cdot \frac{(z_e - z)}{(z_e - z_m)} \quad z_e < z < z_m \tag{1}$$

$$Q_2(x,y,z) = \frac{6\beta_2 \cdot P}{\pi H_2 (r_m^2 + r_m r_i + r_i^2)} exp\left(-2\frac{r^2}{r_0^2}\right), \quad r_0(z) = r_m - (r_m - r_i) \cdot \frac{(z_m - z)}{(z_m - z_i)} \quad z_m < z < z_i \tag{2}$$

where, r_e, r_m and r_i are the radius at the top, middle and bottom, respectively, $r = \sqrt{\xi(t)^2 + \psi(t)^2}$, where ξ and ψ are the coordinates of the local systems moving in the xy plane along the welding path at a constant laser source speed v_0, and z_e, z_m, z_i are the upper, medium and lower plane of the source, respectively. The welding path is described by the position as a function of time of the local reference system described by the coordinates ($x_0(t)$, $y_0(t)$). For a straight welding path along y direction, $x_0(t)$ = cost and $y_0(t) = Y_0 + vt$ (with Y_0 initial position of the source and v the welding speed). The same power P is defined in both the sources given by Eqs. (1) and (2). However, the total absorbed energy (βP, where β is the laser-beam absorptivity) is split into two parts by using different absorption coefficients for the two conical heat sources:

$$\beta P = (\beta_1 + \beta_2) \cdot P \tag{3}$$

For geometrical and loading symmetry reasons, only one half of the joint was modelled using 32480 8-nodes brick finite elements. To capture the high thermal gradient induced by the high-power density welding process, a mesh with a graduated density was adopted, being the lowest element size 0.2 mm along the thickness (fig. 2).

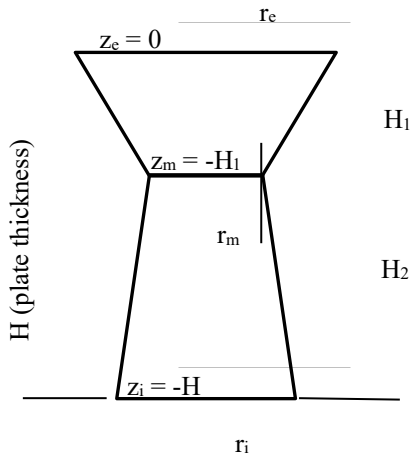

Fig. 1. Volumetric heat source superposition and local reference system moving along the y direction at a speed v.

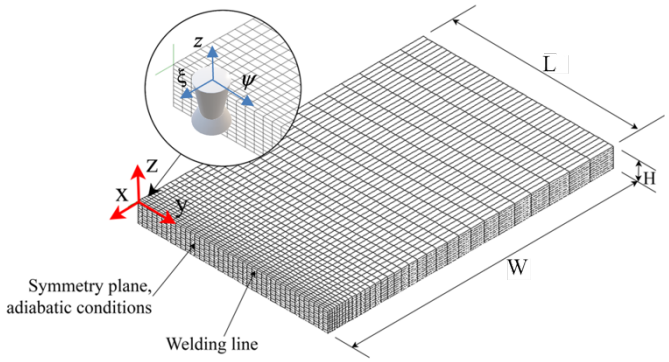

Fig. 2. Numerical model (mesh) with reference system and geometrical parameters.

Exploiting the symmetry of load and geometry, adiabatic condition was applied to the symmetry plane shown in Fig. 2. Convective heat transfer coefficient (h_c) and the emissivity of the material were set to 25 [W/(m^{2}K)] (Solomon et al., 2018) and 0.7, respectively. Physical and thermal material properties were taken as a function of temperature from ThermoClac® database. To consider the latent heat produced during the liquid to solid transformation (and vice versa) the apparent heat capacity approach was used (Zeli et al., 2012).

Following the CWM approach, the temperature history calculated at each node of the numerical model is used as input load for the mechanical computation (uncoupled thermomechanical analysis). The kinematic strain hardening model was chosen while clamping condition was imposed as isostatic. Thermo-mechanical properties as a function of temperature were taken from the report of Nickel Institute and the work by Du et al. (2018). Finally, to simulate the effect of fusion zone in mechanical computation, a function is used that deletes the mechanical history of those elements that reach the solidus temperature of the alloy

3. Numerical results

3.1. Thermal results

The geometrical parameters of the heat source were calculated by numerical run trials aimed at matching the numerical and experimental weld pool shapes. Some parameters of the laser source, such as P and v, are those used in BoP tests. The values of H_1 and H_2 (Fig. 1) are calculated by using a macrograph of the cross section of the bead. Therefore, the only unknown parameters to calibrate via numerical run trials are β_1, β_2, r_e, r_m and r_i (Eqs. (1) and (2)). Best results were obtained by using the parameters collected in Tab 2.

Table 2. Laser welding source parameters.

Source	P (W)	v (mm/s)	r_e (mm)	r_m (mm)	r_i (mm)	H	β
1	1250	25	1.8	0.25	-	0.8	0.4
2	1250	25	-	0.25	0.44	1.2	0.3

Fig. 3 shows the good match obtained between the experimental and numerical shape of the weld pool with parameters reported in Tab 2.

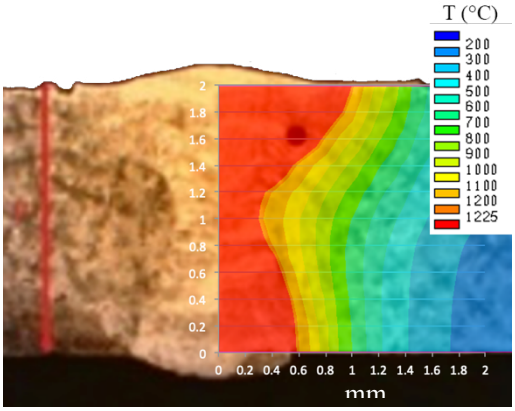

Fig. 3. Matching between experimental and numerical results about weld pool shape (red zone) obtained with a pre-heating of 200 °C

3.2. Pre-heating effect on weld pool morphology and residual stress

As expected, by keeping constant the laser source parameters (power and welding speed), the FZ dimension increases as the pre-heating temperature (P-HT) increases (Fig. 4a). Finally, by using as target value for the FZ shape and dimension the experimental results obtained with the P-HT of 200 °C, the laser power was adjusted to keep constant the FZ width (Fig. 4b). In this case, it was numerically found a linear relation between the laser power (P) and the pre-heating temperature (P-HT) (Eq. 4):

$$P=-A\cdot P\text{-}HT+B \tag{4}$$

where P is the laser power [W], P-HT is the pre-heating temperature [°C], A and B are constants equal to 0.932 [$W°C^{-1}$] and 1435 [W], respectively, calculated by keeping constant the welding speed (v = 25 mm/s).

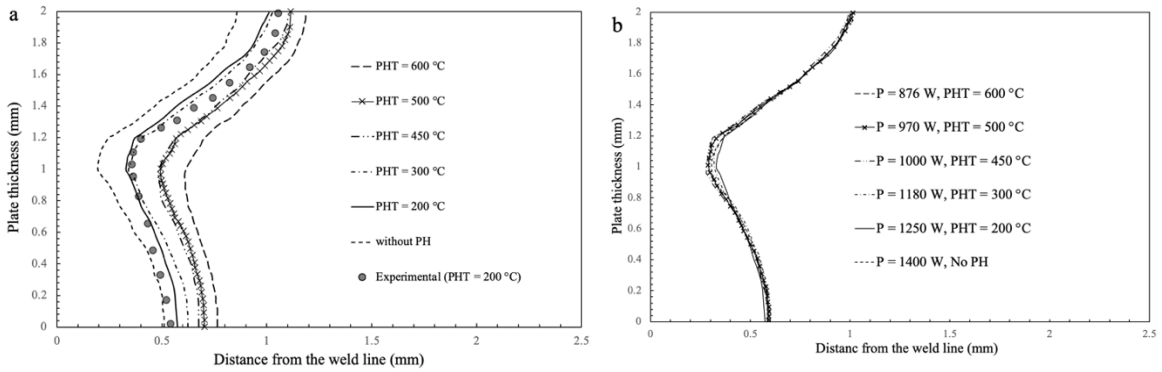

Fig. 4. Shape and dimension of weld pool in the cross section obtained by the numerical model as a function of pre-heating temperature (P-HT): (a) by keeping constant power and welding speed (P = 1250 W, v = 25 mm/s); (b) by adjusting the laser power (via Eq. 4) to keep constant the weld pool width

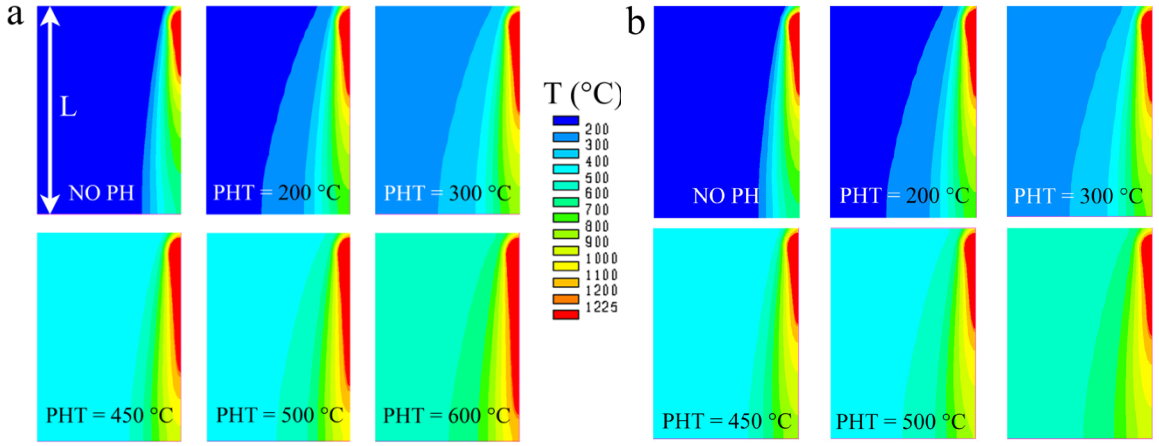

Fig. 5. Temperature map highlighting the weld pool tail as a function of pre-heating temperature: a) by keeping constant welding parameters (P = 1250 W, v = 25 mm/s); b) by adjusting the laser power (via Eq. 4) to keep constant the weld pool width. L = 20 mm

At constant laser welding parameters, also the weld pool tail length increases as the P-HT increases (Fig. 5a); on the other hand, by adjusting the laser power (through Eq. 4) to keep the weld pool width constant, the weld pool tail length tends to remain quite constant, with only a slightly increases as the P-HT increases (Fig. 5b).

Only the distribution of the longitudinal residual stress (RS) will be reported below as it has the highest values compared to the other components. Longitudinal residual stress distribution is reported in Figs. 6 and 7 as a function of the pre-heating temperature. The analyses were carried out by both keeping power and welding speed (P = 1250 W, v = 25 mm/s) constant and adjusting only the laser power to keep the weld pool shape and dimension constant.

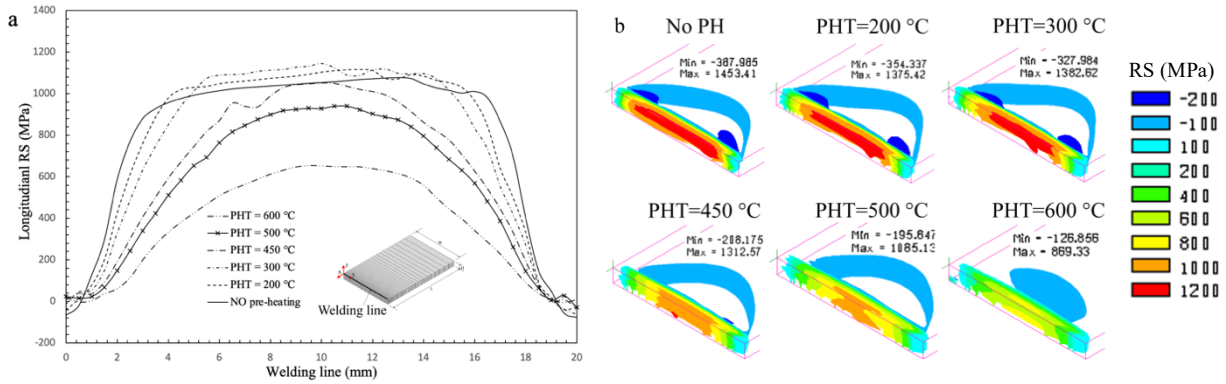

Fig. 6. Longitudinal RS (MPa): (a) along the welding line and (b) in form of 3D iso-stress surfaces as a function of P-HT. Power and welding speed were kept constant (P = 1250 W, v = 25 mm/s). Geometrical parameters (Fig. 2): H = 2 mm, W = 15 mm, L = 40 mm.

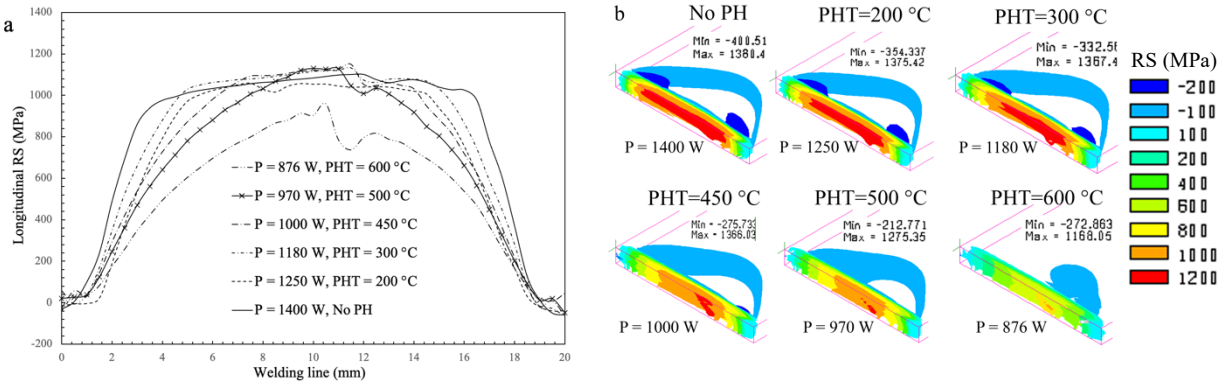

Fig. 7. Longitudinal RS (MPa) (a) along the welding line and (b) in form of 3D iso-stress surfaces as a function of P-HT calculated by keeping constant the weld pool dimension and shape. Geometrical parameters (Fig. 3): H = 2 mm, W = 30 mm, L = 20 mm.

If welding parameters (power and welding speed) are kept constant (Fig. 6), the iso-stress surface characterized by the maximum RS values (red area in fig. 6b) tends to de-crease as the P-HT increases (starting from the boundaries); however, to see a significant reduction in the maximum value of residual stresses, the preheat temperature should exceed 500 °C (Fig. 6a) in agreement with the work by Suharno and Sugianto (2012). Finally, the higher the preheating temperature, the lower the plateau extension of the longitudinal RS distribution along the welding line (Fig. 6a) and starting from a preheating temperature of 450 °C the plateau disappears. It can be argued that such behaviour is induced by boundary effects and is related to the ratio between the FZ tail length (Fig. 5a) and the plate length (L). It is in fact noted that the longest plateau is reached with the lowest value of the above-mentioned ratio in combination with a lower P-HT, since stationary conditions are reached more easily.

By keeping the weld pool constant, again the higher the P-HT, the lower the overall RS values. However, by focusing on the distribution of longitudinal RS along the weld line (Fig. 7a), it is found that a significant RS reduction starts using a P-HT over 500 °C. Comparing Figs. 6 and 7, it is observed that, with constant preheating, increasing the laser power reduces the RS values, starting from P-HT = 450 °C. It is worth mentioning that the reference case that

was considered in this numerical analysis is the experimental one (P-HT = 200 °C, P = 1250 W) that is therefore the same in Fig. 6 and Fig. 7.

3.3. Effect of welding speed

In the following, the welding speed was reduced to 20 mm/s to assess its influence on RS. Laser power was kept both constant (P = 1250 W) and reduced to 1000 W to obtain the same heat input (P/v) of previous analyses. For the sake of simplicity, only the longitudinal residual stresses are reported in Fig. 8 as a function of P-HT.

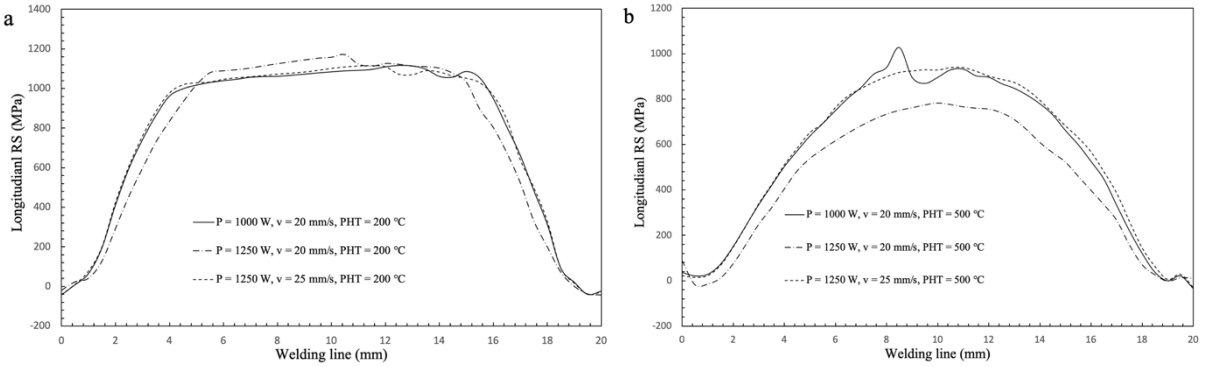

Fig. 8. Influence of welding speed on longitudinal RS as a function of laser power and pre-heating temperature: a) 200 °C, b) 500 °C

It is observed that at 200 °C the reduction of welding speed has not benefit in terms of RS value reduction. On the other hand, at 500 °C a significant RS value reduction is associated with the lowest welding speed (20 mm/s) in combination with the highest laser power (1250 °C). In this condition the results are comparable to those predicted with a P-HT of 600 °C, P = 1250 W and v = 25 mm/s (Fig. 6). Further investigations were carried out by reducing the welding speed more significantly to 5 mm/s while setting P-HT at 400 °C. The laser power was set both at 1250 W and 250 W to compare the results keeping the heat input constant. Results are summarized in Figure 9.

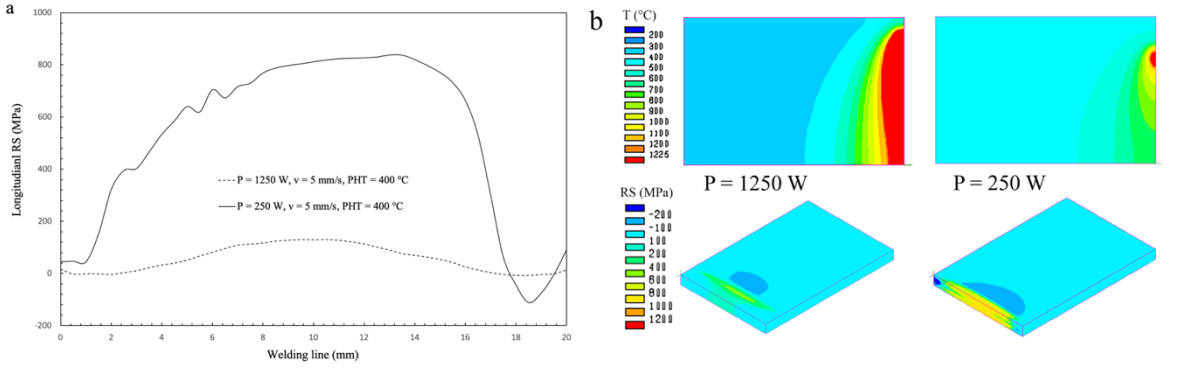

Fig. 9. Thermal and mechanical results as a function of laser power (P) with welding speed 5 mm/s, P-HT 400 °C, thickness 2 mm.

Despite the lower value of the P-HT, compared to previous results (Fig. 8), the reduction of laser speed to 5 mm/s reduces the RS field both keeping the power constant at 1250 W and reducing it to 250 W to maintain the same heat input of original data (say, P = 1250 W and speed 25 mm/s). The combination P = 1250 and v = 5 mm/s has the major effect in reducing the residual stress.

The welding speed influences the growth direction of dendrites during solidification, which could play an important role in the solidification cracking phenomenon. The grain growth rate is proportional to the cooling rate (DuPont, 2011) [16]. If θ is the angle between the laser scan speed (v) direction and the solidification direction, the solidification rate, R, is given by (Zhanga and Zhang, 2019):

$$R=v\cdot\cos\theta \tag{5}$$

Thus, $R \approx 0$ at the fusion line at the two sides of the melt pool and R = v at centerline. The higher the scan speed the lower the grain size due to higher cooling rate. Depending on process parameter the grain structure type can be that due to ‘competitive grain growth’ where the grains at the fusion line are oriented in a favourable direction for growth but other grains may surpass the first ones as the fusion line changes its orientation. As a result, the grains at the centerline will grow toward the laser direction. The other grain structure type is called ‘centerline grain boundary forming’. In this case, grains grow straight from the fusion line to the centerline until they touch each other forming the centerline grain boundary. It is found (Zhanga and Zhang, 2019) that by increasing the scan speed, the microstructure changes from ‘competitive grain growth’ to ‘centerline grain boundary forming’.

Another important feature influencing solidification cracking (SC) is the extension of the so-called crack-susceptible zone (CSZ) defined as the zone that extends usually from the coherency (Tc) to the solidus (Ts) temperature range. Here, for the sake of simplicity it is considered the coherency temperature equal to the liquidus temperature. The higher the CSZ, the higher the risk of SC. Using the Rosenthal equation for calculating the temperature distribution induced by a point source, in full penetration mode is it possible to estimate the CSZ size (x, in fig. 10) by Eq. (6):

$$x = \pi\alpha\frac{P^2}{v}\left(\frac{1}{2\pi Kh}\right)^2\left[\frac{1}{(T_s-T_0)^2}-\frac{1}{(T_c-T_0)^2}\right] \tag{6}$$

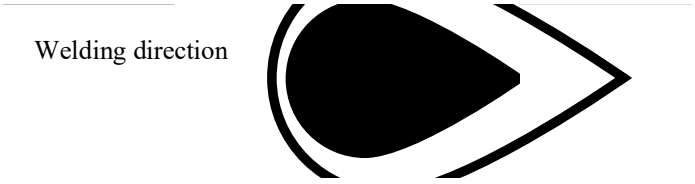

Fig. 10. Schematic of CSZ extension (x)

Where Ts and Tc are the lower and upper temperatures respectively (Fig. 10), T_0 is the reference temperature (or preheating temperature), α is the thermal diffusivity, K is the thermal conductivity, and h is the plate thickness. It is interesting to note that keeping the heat input (P/v) constant, the CSZ size increases as the welding speed (v) increases as shown in Fig. 11. The time t_s within the CSZ, i.e., to drop temperature from Tc to Ts, is simply given by:

$$t_s = \frac{CSZ}{v} \tag{7}$$

that, according to Eq. (6), results proportional to the square of heat input, $(P/v)^2$ and therefore constant in Fig. 11. It is the time available for backfilling, i.e., liquid feeding of the opening mushy. Consequently, different solidification cracking behaviours are expected when changing welding conditions because of the associated changes in CSZ lengths and available backfilling time. Since t_s doesn't change at constant heat input (HI), it is supposed that the lowest risk of hot cracking could be reduced by reducing the CSZ size and therefore, for a fixed value of HI, reducing the welding speed. It is observed in Fig. 11 that the higher the P-HT the higher the CSZ size but even t_s increases proportionally.

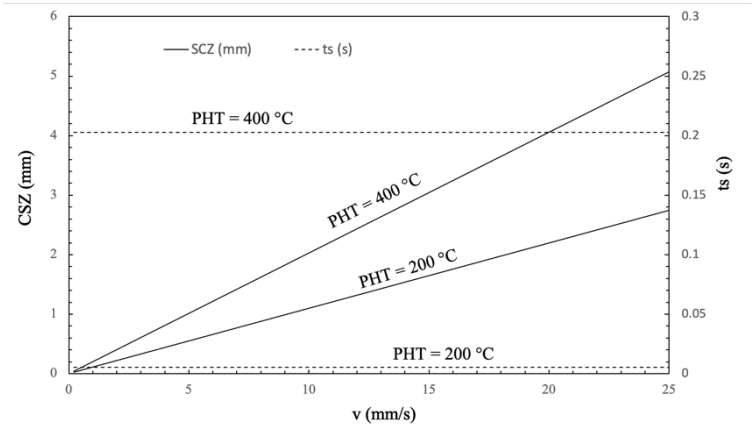

Fig. 11. CSZ and t_s as a function of welding speed for a 2 mm thickness IN972 plate, laser butt welded at a constant value of heat input equal to 50 J/mm, h = 2 mm, P-HT = 200 °C and 400 °C.

Interestingly, if the laser power is kept constant, an opposite effect of welding speed on CSZ size is predicted by using the Rosenthal equation (Fig. 12). At constant power, the higher the welding speed the lower the CSZ and thus the hot cracking susceptibility. Again, the higher the P-HT, the higher the CSZ size and t_s, but in this case t_s decreases with the welding speed.

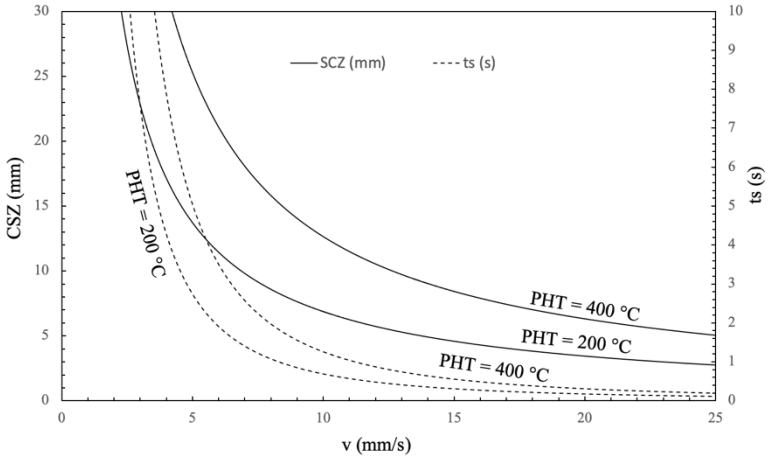

Fig. 12. CSZ and t_s as a function of welding speed for a 2 mm thickness IN972 plate, laser butt welded at a constant value of power (P) equal to 1250 W, h = 2 mm, P-HT = 200 °C and 400 °C.

A thermomechanical simulation was carried out with a welding speed of 5 mm/s and results were compared with those obtained using a welding speed of 25 mm/s, keeping the same heat input (P/v), 50 J/mm. The focus was on the dimension of mushy zone (MZ) in relation with its stress and strain field (in the longitudinal direction) promoting transversal SC. Fig. 13 shows a comparison between the temperature-stress filed in 5 mm/s and 25 mm/s laser welding, while in Fig. 24 the temperature and longitudinal stress along the welding line is plotted for the two welding speeds.

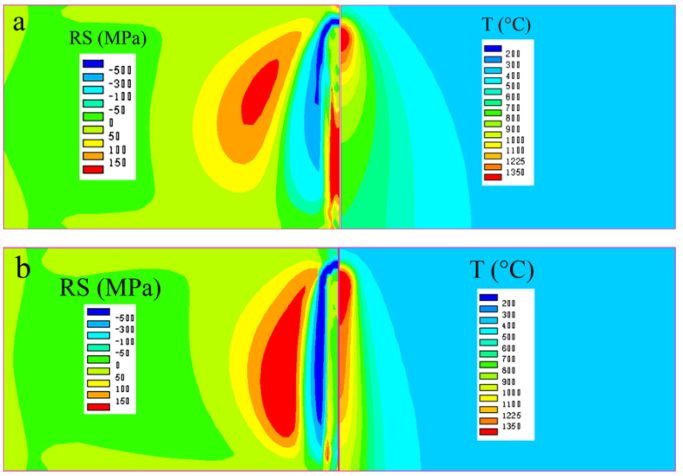

Fig. 13. Comparison between the temperature-stress filed in 5 mm/s (a) and 25 mm/s (b) laser welding of IN792, thickness 2 mm, P-HT = 400 °C (W = 30, L = 20)

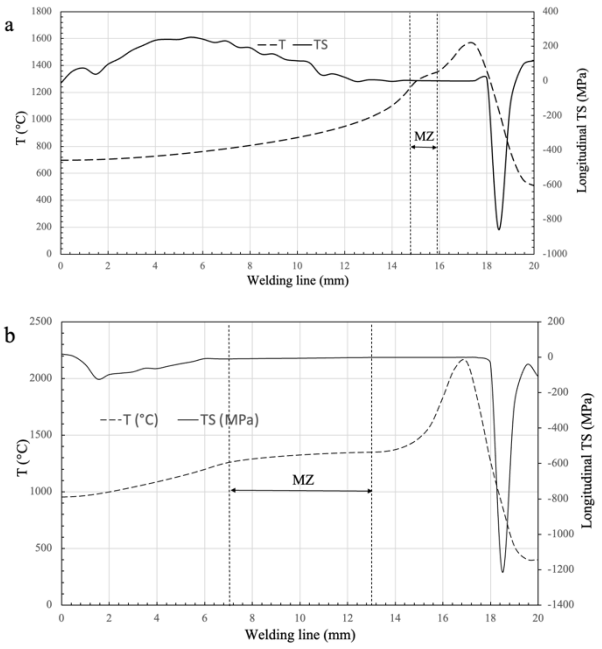

Fig. 14. Comparison between the temperature-stress filed in 5 mm/s (a) and 25 mm/s (b) laser welding of IN792, thickness 2 mm, P-HT = 400 °C

Both figure 13 and 14 highlight the great variation of mushy zone (MZ) size moving from 5 mm/s to 25 mm/s welding speed with the lowest value for the 5 mm/s welding speed. However, in MZ the longitudinal stress is positive and about 1.5 MPa, while using the 25 mm/s welding speed, in the corresponding MZ a compressive RS stress is calculated, equals to about -10 MPa. Even the thermal stresses in the sub-solidus zone are extremely different (tensile in Fig. 14a and compressive in Fig. 14b) and can play a role in hot cracking formation.

3.4. Effect of butt-welded joint geometry on longitudinal residual stress

By keeping constant the plate thickness (2 mm), P-HT (500 °C) and welding parameters (P = 1250 W, v = 25 mm/s), both the width (W) and the length (L) of the plate were varied with the aim to study their influence on longitudinal RS (σ_{yy}). Results are summarized in Fig. 15. By observing Figs. 15a and 15b, no influence of the width (W) on the longitudinal RS distribution is observed. On the other hand, by doubling the joint length the RS increases and reach a plateau along the welding line (Figs. 15c and 15d) which value is in the range of those observed in Figs. 6 and 7 for P-HT lower than 450 °C.

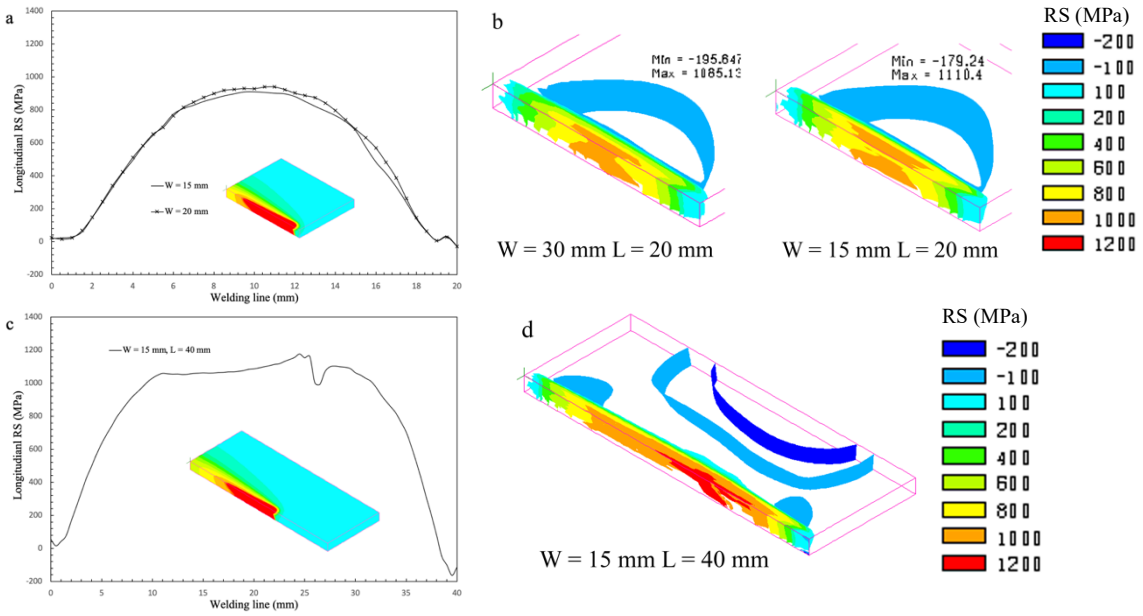

Fig. 15. Longitudinal residual stress (MPa) as a function of geometrical parameters of the welded joint with P-HT = 500 °C: a,b) W = 30÷15 mm and L = 20 mm; c,d) W = 30 mm and L = 40 mm (P = 1250 W, v = 25 mm/s)

Further parametric analyses were carried out by rising the P-HT to 600 °C to search for RS reduction even in the 40 mm length plate, both at constant laser power (1250 W) and constant weld pool width, as described above. It was found that by keeping laser parameters constant, the P-HT of 600 °C effectively reduces the RS (compare Fig. 15 with Fig. 16) even if a high RS peak (above 1200 MPa) remains. By reducing the laser power to maintain constant the FZ width (Fig. 16), RS at P-HT of 600 °C tends to be comparable with that obtained at P-HT = 500 °C but with a higher power.

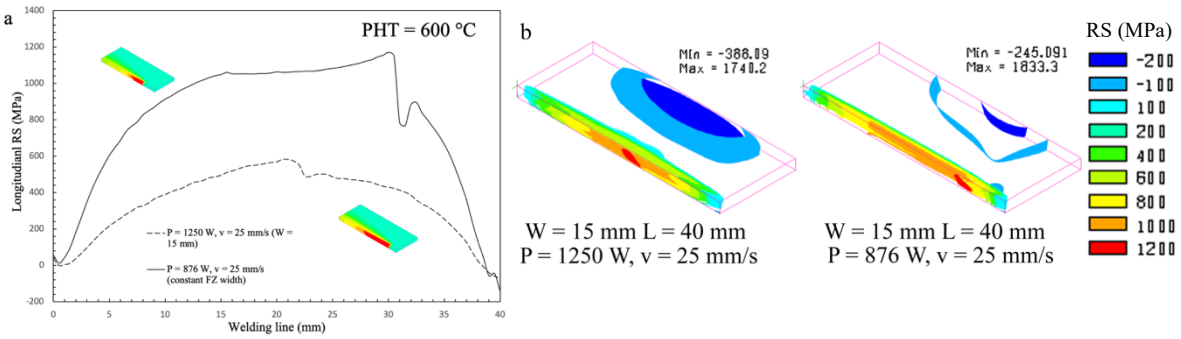

Fig. 16. Longitudinal residual stress as a function of laser power with P-HT = 600 °C: a) distribution along the welding line; b) 3D iso-stress surfaces (MPa)

4. Preliminary experimental results

Some BoP trials were carried out according to parameters summarized in Fig. 17 on IN792 plates in the equiaxed grain state.

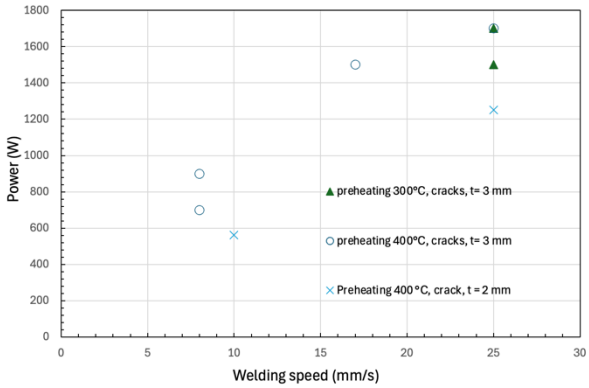

Fig. 17. Parameters used in BoP trials

Unfortunately, no parameters combination resulted in sound welds. Transversal cracking was the main drawback, as shown in Fig. 18.

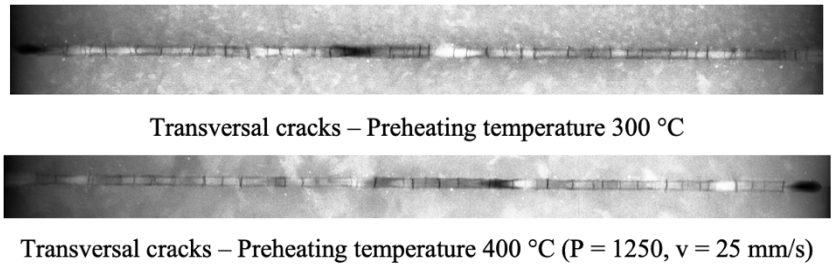

Fig. 18. Transversal cracks in the weld beads after laser BoP tests

As discovered by numerical simulations, apparently no combination of parameters leads to simultaneous minimization of thermal stresses in CSZ and CSZ size. A preheating of 400 °C is still insufficient to avoid the presence of solidification cracks as indicated by Suharno and Sugianto (2012), as well. However, it should be noted that the use of preheats above 500 °C, the only ones that can reduce welding stress significantly, are also difficult to manage in laser welding and other strategies should therefore be considered before increasing the preheating temperature, such as the use, for example, of a double heat source as indicated in literature (Hu and Richardson, 2006).

5. Conclusions

A laser welding numerical model of IN792 was developed with the aim at assessing the influence of process parameters on thermal field, thermal and residual stresses. Moreover, some preliminary 'bead-on-plate' trials were carried out to evaluate the laser weldability of the investigated alloy in the equiaxed grain state. The main outcomes can be summarised as follows:

- IN792, in the equiaxed grain state, has a very low weldability. It is affected by transversal cracking.
- According to simulation and literature, P-HT over 500 °C should be necessary to significantly reduce residual and thermal stresses and obtain sound welds.
- Since it is difficult to operate at so high P-HT, it is suggested in the future to investigate the use of a double heat source (laser-laser or arc-laser).
- Effect of welding speed is controversial: lower welding speeds reduce the CSZ extension but increase the thermal stress, above all in the sub-solidus zone, and 'vice versa' for higher welding speeds.

To better understand which further mitigating actions could be necessary to operate to obtain sound weldments, EBSD and SEM analyses will be carried out on welding cracks to find information about their origin (solidification cracking or sub-solidus weld cracking) and the different behaviour between the equiaxed grain alloy and the directionally solidified one.

Acknowledgements

Founding: This work was supported by PRIN 2022 project, ELAPSE: Laser Welding and Repair of Superalloys (project 20225YNH4M). ELAPSE is financed by European Union through PNRR founds.

References

Angella, G.; Barbieri, G.; Donnini, R.; Montanari, R.; Richetta, M.; Varone, A. 2017. Electron Beam Welding of IN792 DS: Effects of Pass Speed and PWHT on Microstructure and Hardness. Materials 2017, 10, 1033. https://doi.org/10.3390/ma10091033

Barbieri, G.; Cognini, F.; de Crescenzo, C.; Fava, A.; Moncada, M.; Montanari, R.; Richetta, M.; Varone, A. 2024. Process Optimization in Laser Welding of IN792 DS Super-alloy. Metals 2024, 14, 124. https://doi.org/10.3390/met14010124

Coniglio N, Cross CE. 2020. Effect of weld travel speed on solidification cracking behavior. Part 1: weld metal characteristics. Int J Adv Manuf Technol 2020;107:5011–5023. https://doi.org/10.1007/s00170-020-05231-y

Coniglio N, Cross CE. 2020. Effect of weld travel speed on solidification cracking behavior. Part 2: testing conditions and metrics. Int J Adv Manuf Technol 2020;107:5025–5038. https://doi.org/10.1007/s00170-020-05232-x

Coniglio N, Cross CE. 2020. Effect of weld travel speed on solidification cracking behavior. Part 3: modeling. Int J Adv Manuf Technol 2020;107:5039–5051. https://doi.org/10.1007/s00170-020-05233-w

David S.A., Babu S.S., Vitek J.M. 1997. Weldability and Microstructure Development in Nikel-Base Superalloys. Proceedings of the Conference on 'Numerical Analysis of Weldability – V'. Graz, Austria.

Du, B., Sheng, L. , Hu, Z., Cui, C., Yang, J., and X. Sun. 2018. Investigation on the micro-structure and tensile behavior of a Ni-based IN792 superalloy. Advances in Mechanical Engineering 2018, Vol. 10(2) 1–8. DOI: 10.1177/1687814017752167

DuPont, J.N. 2011. Fundamentals of weld solidification, ASM Handbook 6A, pp. 96–113.

Hu, B., Richardson, I.M. 2006. Mechanism and possible solution for transverse solidification cracking in laser welding of high strength aluminum alloys. Materials Science and Engineering A 429 (2006) 287–294.

Nikel Institute https://nickelinstitute.org/media/8d93486143182f5/nickel_incopub393_updated-june-2021.pdf

Norouzian, M., Elahi, M.A, Plapper, P. 2023. A review: Suppression of the solidification cracks in the laser welding process by controlling the grain structure and chemical compositions, Journal of Advanced Joining Processes, Vol 7, 2023, 100139, https://doi.org/10.1016/j.jajp.2023.100139.

Rinaldi, C., Gavito, L., Gerelli, I., Singleton, P., Walker, P., Guardamagna, C., Moscot-ti, L., Bayard, P., Bertoli, A. 1997. Automatic refurbishment of gas turbine components by CO2 robot laser' Proc. Conf. 'Materials Solutions 1997 on joining and repair of gas turbine components'. Indianapolis, USA, 15-18 September 1997 109-117. Publ. ASM, Materials Park, USA

Sandy, D., Frederick, G., Peterson, A., Stover, J., Viswanathan, R. 2000. Development of a laser-based/high strength weld filler process to extend repair limits on IN738 gas tur-bine blades. Proc. Conf. 'Welding and Repair Technology for Power Plants - EPRI 2000', 7-9 June 2000, Marco Island, USA. Publ: Electric Power Generation Institute, Charlotte, USA, 2000. Paper P05-GI.

Solomon, A.S., Aravinthan, G., Deepak, R., Kishore Kumar, M., Anantha Padmanaban, M.R. 2018. Simulation and Modeling of the Effect of Welding Process Parameters of Inconel 625. International Journal of Engineering Research & Technology, 6(7) 1-6.

Suharno, Dr., Sugianto, A. 2012. Advantage of SWET Technique on Joining Inconel 792 Material. Global Journals of Research in Engineering, 12(A6), 21–26.

Wilson, J. Michael et al. 2014. Remanufacturing of turbine blades by laser direct deposition with its energy and environmental impact analysis. Journal of Cleaner Production 80 (2014): 170-178.

Zeneli, M., Nikolopoulos, N., Karellas, S., Nikolopoulos, N. 2021. Chapter 7 - Numerical methods for solid-liquid phase-change problems, Editor(s): Alejandro Datas, In Woodhead Publishing Series in Energy, Ultra-High Temperature Thermal Energy Storage, Transfer and Conversion, Woodhead Publishing, 2021, Pages 165-199, ISBN 9780128199558, https://doi.org/10.1016/B978-0-12-819955-8.00007-7

Zhanga, Y., Zhang, J. 2019. Modeling of solidification microstructure evolution in laser powder bed T fusion fabricated 316L stainless steel using combined computational fluid dynamics and cellular automata. Additive Manufacturing, 28, pp. 750–765